

## Improving the resolution of grating-assisted optical diffraction tomography using a priori information in the reconstruction procedure

Patrick C. Chaumet\*, Anne Sentenac, Kamal Belkebir,  
Guillaume Maire and Hugues Giovannini

*Institut Fresnel (UMR 6133), Université d'Aix-Marseille, Avenue Escadrille  
Normandie-Niemen, F-13397 Marseille cedex 20, France*

*(Received 29 October 2009; final version received 22 January 2010)*

We provide a numerical study of a tomographic microscope in which the sample is deposited on a periodically nanostructured substrate and is illuminated under various incident angles. The map of permittivity of the sample is retrieved numerically from the complex data of the diffracted far-field. A single-scattering analysis shows that, with an optimized grating of period  $\lambda/5$ , the transverse resolution of the digital imager is about  $\lambda/10$ . To ameliorate the resolution further, a priori information is incorporated in the inversion procedure. Fixing the lower and upper bounds of the sample permittivity permits us to obtain a transverse resolution about  $\lambda/15$ .

**Keywords:** optical diffraction tomography; gratings; evanescent wave

### 1. Introduction

Optical diffraction tomography (ODT) is a promising digital imaging technique in which the sample permittivity is retrieved numerically from the complex data of the diffracted field obtained for various angles of illumination. This technique has been shown to exhibit a better resolution than that of a standard microscope with the same numerical aperture (NA) [1–3]. Using single scattering analysis, it is shown that the resolution of ODT is about  $0.35\lambda/NA$  [4] while that of the wide-field microscope is equal to the Rayleigh criterion  $0.6\lambda/NA$  [5]. Basically, two approaches can be followed to ameliorate the resolution of ODT.

The first one, which has been primarily adopted for analogical microscopes, consists of diminishing the effective incident wavelength by using immersed objectives or prisms [6–8]. The higher the refraction index  $n$  of the immersion liquid or prism, the smaller the effective wavelength,  $\lambda_{\text{eff}} = \lambda/n$ , and the better the resolution. With the present lossless materials existing in optics, the resolution can be ameliorated by a factor two at best. To overcome this limit, it has been proposed to deposit the sample on a periodically nanostructured substrate. The grating is optimized so as to transform the impinging propagative beam into an evanescent field with high spatial frequency. In this case, the effective wavelength of the field illuminating the sample depends solely on the grating period  $d$  and it can be much smaller than  $\lambda/2$ . Simulations of grating-assisted ODT have shown that

one could expect a resolution about  $\lambda/10$  with this approach [9,10].

The second way to ameliorate the resolution lays on the reconstruction algorithms. Most of the present experimental and theoretical studies of ODT make use of linear inversion algorithms, based on inverse Fourier transforms [1,3,6,11–13] to retrieve the sample permittivity. These techniques yield good results when the sample is weakly diffracting and are particularly adapted to biological issues. Non-linear iterative inversion techniques have also been developed to image highly contrasted samples such as those encountered in the nanotechnology domain [14,15]. The latter provide much better images than that obtained with linear reconstruction algorithms when multiple scattering cannot be neglected [14,15] and they may even ameliorate the resolution beyond that expected with the single scattering analysis [16–18]. Yet, the advantages of numerical imaging have still not been fully exploited. Indeed, up to now, most of the inversion techniques developed for ODT have not incorporated any a priori information on the object. Now, it has been shown, in the microwave domain in particular, that a spectacular amelioration of the images can be obtained just by specifying the lower and upper bounds of the sample permittivity [19].

In this work, we present a numerical study of the resolution of a grating-assisted digital microscope using different inversion procedures. In Section 2 we recall the principles of grating-assisted ODT and we

\*Corresponding author. Email: patrick.chaumet@fresnel.fr

derive the point spread function of the imager using a single scattering analysis. In Section 3, we sketch the numerical technique that is used to simulate the experiment and we detail the reconstruction algorithm that accounts for some a priori information on the object. Lastly, in Section 4, we compare the images obtained with and without a priori information for various samples [16].

## 2. Single-scattering analysis of the resolution of grating-assisted ODT

We consider a tomographic microscope in reflection configuration. The sample (in air) is deposited on a periodically nanostructured glass slide (see Figure 1). Both the illumination and the detection are performed through the glass substrate. Experimentally, this configuration could be realized by using the same immersed objective for the illumination and the detection as in a classical reflection microscope. The grating-substrate is similar to that described in [9,10]. It consists of a 7 nm silver film with  $n_{\text{silver}} = 0.12 + 2.91i$ , and a 7 nm layer of  $\text{SiO}_2$  with  $n_{\text{SiO}_2} = 1.5$  deposited on a glass substrate  $n_s = 1.5$ . The  $\text{SiO}_2$  layer is etched with square holes along a

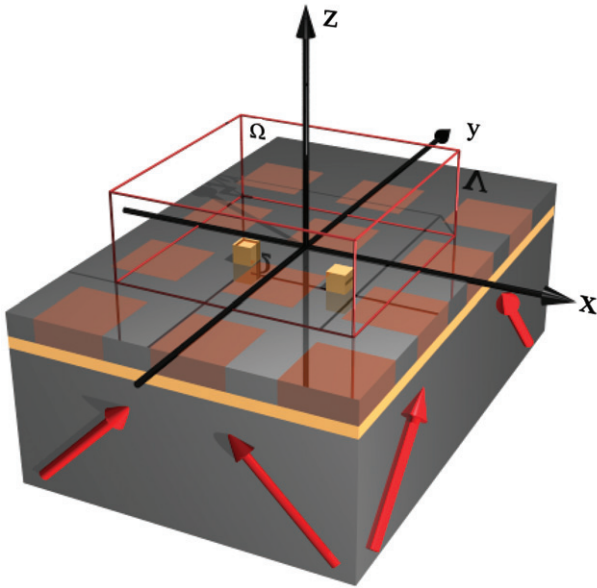


Figure 1. Geometry of the imaging system. The objects are deposited on a nanostructured substrate and successively illuminated from below by eight  $p$  polarized plane waves. The incident angle with respect to  $z$  axis is always  $80^\circ$  while the incident angle with respect to  $x$  axis varies with a step of  $45^\circ$ . The far-field is detected in the substrate along 80 directions equally spaced within a cone of half-angle  $70^\circ$ . (The color version of this figure is included in the online version of the journal.)

square mesh. The holes are filled with  $\text{Ta}_2\text{O}_5$ , with  $n_{\text{Ta}_2\text{O}_5} = 2.1$ . The period  $d$  of the square grating along the  $x$  and  $y$  axes is 100 nm while the side of the holes is 67 nm and the free-space wavelength of illumination  $\lambda = 500$  nm. When the grating is illuminated by a plane wave with tangential wavevector  $\mathbf{k}_{\text{inc}}$  and linear polarization  $\hat{\mathbf{u}}$ , the transmitted electric field above the grating can be written as a Rayleigh series,

$$\mathbf{E}_{\text{grating}}(\mathbf{k}_{\text{inc}}, \hat{\mathbf{u}}, \mathbf{r}_{\parallel}, z) = \exp(i\mathbf{k}_{\text{inc}} \cdot \mathbf{r}_{\parallel}) \sum_{n,m} \mathbf{A}_{n,m}(\mathbf{k}_{\text{inc}}, \hat{\mathbf{u}}) \times \exp(i\mathbf{K}_{n,m} \cdot \mathbf{r}_{\parallel} + ik_z^{n,m} z) \quad (1)$$

where  $\mathbf{K}_{n,m} = n2\pi/d\hat{\mathbf{x}} + m2\pi/d\hat{\mathbf{y}}$ ,  $k_z^{n,m} = [k_0^2 - |\mathbf{K}_{n,m} + \mathbf{k}_{\text{inc}}|^2]^{1/2}$  with the imaginary part of  $k_z^{n,m}$  positive,  $k_0 = 2\pi/\lambda$  and  $\mathbf{r} = (\mathbf{r}_{\parallel}, z)$ . The period of the grating being much smaller than  $\lambda$ , the grating behaves in most cases as a homogeneous layer and only the  $(0, 0)$  order is dominant in the series. In this case, the field just above the grating can be approximated by,

$$\mathbf{E}_{\text{grating}}(\mathbf{k}_{\text{inc}}, \hat{\mathbf{u}}, \mathbf{r}_{\parallel}, 0) \approx \mathbf{A}_{0,0}(\mathbf{k}_{\text{inc}}, \hat{\mathbf{u}}) \exp(i\mathbf{k}_{\text{inc}} \cdot \mathbf{r}_{\parallel}). \quad (2)$$

However, thanks to the thin metallic layer, the grating also supports electromagnetic eigenmodes (short-range and long-range plasmons) which can be excited for specific tangential incident wavevectors. In this case, the Rayleigh series contains at least two dominant terms [10]. For example, when the grating is illuminated by a  $p$ -polarized plane wave with tangential wavevector  $\mathbf{k}_{\text{res}} = n_s \frac{2\pi}{\lambda} \sin \theta_{\text{res}} \hat{\mathbf{x}}$  with  $\theta_{\text{res}} \approx 80$  degree, the field just above the grating can be written as,

$$\mathbf{E}_{\text{grating}}(\mathbf{k}_{\text{res}}, \hat{\mathbf{p}}, \mathbf{r}_{\parallel}, 0) \approx \exp(i\mathbf{k}_{\text{res}} \cdot \mathbf{r}_{\parallel}) [\mathbf{A}_{0,0}(\mathbf{k}_{\text{res}}, \hat{\mathbf{p}}) + \mathbf{A}_{-1,0}(\mathbf{k}_{\text{res}}, \hat{\mathbf{p}}) \exp(i\mathbf{K}_{-1,0} \cdot \mathbf{r}_{\parallel})], \quad (3)$$

where  $\hat{\mathbf{p}}$  denotes the linear  $p$ -polarization of the incident plane wave that corresponds to an incident electric field in the plane of incidence. The amplitude of the  $(-1, 0)$  order is dominant in the Rayleigh series at this angle of incidence because it corresponds to the excitation through the  $(-1, 0)$  reciprocal wavevector of the short-range plasmon supported by the metallic film. We have checked with a rigorous calculation of the grating field with a Fourier modal method [20] that, in this configuration, all the orders in the Rayleigh series are at least ten times smaller than the  $(0, 0)$  order, except the  $(-1, 0)$  order which is about half the zero order.

We now study the field diffracted by an object, described by its relative permittivity  $\varepsilon(\mathbf{r}_{\parallel}, z)$ , which is deposited on the grating. The whole structure is illuminated by a  $\hat{\mathbf{u}}$ -polarized plane wave stemming from the substrate with tangential wavevector  $\mathbf{k}_{\text{inc}}$ . Under the renormalized Born approximation, the far-field  $\mathbf{e}(\mathbf{k}_d, \mathbf{k}_{\text{inc}}, \hat{\mathbf{u}})$  diffracted by the object along

the direction defined by the tangential wavevector  $\mathbf{k}_d$  reads,

$$\mathbf{e}(\mathbf{k}_d, \mathbf{k}_{\text{inc}}, \hat{\mathbf{u}}) \approx \int \alpha_d(\mathbf{r}_{\parallel}, z) \mathbf{g}(\mathbf{k}_d, \mathbf{r}_{\parallel}, z) \times \mathbf{E}_{\text{grating}}(\mathbf{k}_{\text{inc}}, \hat{\mathbf{u}}, \mathbf{r}_{\parallel}, z) d\mathbf{r}_{\parallel} dz \quad (4)$$

where  $\alpha_d$  is the density of polarizability of an infinitely small spherical or square material volume of the object, given by

$$\alpha_d(\mathbf{r}_{\parallel}, z) = \frac{3}{4\pi} \frac{\varepsilon(\mathbf{r}_{\parallel}, z) - 1}{\varepsilon(\mathbf{r}_{\parallel}, z) + 2}, \quad (5)$$

and  $\mathbf{g}(\mathbf{k}_d, \mathbf{r}_{\parallel}, z) \cdot \mathbf{p}$  is the far-field radiated in the substrate along the direction defined by the tangential wavevector  $\mathbf{k}_d$  by a dipole  $\mathbf{p}$  placed at  $\mathbf{r} = (\mathbf{r}_{\parallel}, z)$  above the grating. Invoking the reciprocity theorem, [21–23], the  $\hat{\mathbf{v}}$  component of  $\mathbf{e}(\mathbf{k}_d, \mathbf{k}_{\text{inc}}, \hat{\mathbf{u}})$  can be written as,

$$\mathbf{e}(\mathbf{k}_d, \mathbf{k}_{\text{inc}}, \hat{\mathbf{u}}) \cdot \hat{\mathbf{v}} \approx \int \alpha_d(\mathbf{r}_{\parallel}, z) \times \mathbf{E}_{\text{grating}}(-\mathbf{k}_d, \hat{\mathbf{v}}, \mathbf{r}_{\parallel}, z) \mathbf{E}_{\text{grating}}(\mathbf{k}_{\text{inc}}, \hat{\mathbf{u}}, \mathbf{r}_{\parallel}, z) d\mathbf{r}_{\parallel} dz. \quad (6)$$

For sake of simplicity, we assume that  $\varepsilon(\mathbf{r}_{\parallel}, z) - 1 = \Delta\varepsilon(\mathbf{r}_{\parallel})H(z)$  where  $H$  is equal to zero for  $z > h$  and  $z < 0$  and is equal to one for  $0 < z < h$  with  $h$  much smaller than the wavelength. Under these assumptions, if both the detection and illumination are achieved under non-resonant conditions, one gets,

$$\mathbf{e}(\mathbf{k}_d, \mathbf{k}_{\text{inc}}, \hat{\mathbf{u}}) \cdot \hat{\mathbf{v}} \approx h \tilde{\alpha}_d(\mathbf{k}_{\text{inc}} - \mathbf{k}_d) \mathbf{A}_{0,0}(-\mathbf{k}_d, \hat{\mathbf{v}}) \cdot \mathbf{A}_{0,0}(\mathbf{k}_{\text{inc}}, \hat{\mathbf{u}}), \quad (7)$$

where  $\tilde{\alpha}$  is the 2D Fourier transform of  $\alpha(\mathbf{r}_{\parallel}, 0)$ . If the illumination is achieved under the resonant conditions, Equation (3), while the detection is achieved under non-resonant conditions, Equation (2), one gets,

$$\mathbf{e}(\mathbf{k}_d, \mathbf{k}_{\text{res}}, \hat{\mathbf{p}}) \cdot \hat{\mathbf{v}} \approx h \left[ \tilde{\alpha}_d(\mathbf{k}_{\text{res}} - \mathbf{k}_d) \times \mathbf{A}_{0,0}(-\mathbf{k}_d, \hat{\mathbf{v}}) \cdot \mathbf{A}_{0,0}(\mathbf{k}_{\text{res}}, \hat{\mathbf{p}}) + \tilde{\alpha}_d(\mathbf{k}_{\text{res}} + \mathbf{K}_{-1,0} - \mathbf{k}_d) \times \mathbf{A}_{0,0}(-\mathbf{k}_d, \hat{\mathbf{v}}) \mathbf{A}_{-1,0}(\mathbf{k}_{\text{res}}, \hat{\mathbf{p}}) \right]. \quad (8)$$

In this case, the scattered field is linked to two Fourier coefficients of the object polarizability. Yet, it is generally possible to find both frequencies, by taking another incident wavevector  $\mathbf{k}_{\text{inc}}$ , and another direction of observation  $\mathbf{k}'_d$  so that  $\mathbf{k}_{\text{res}} - \mathbf{k}_d = \mathbf{k}_{\text{inc}} - \mathbf{k}'_d$ . We can now define the Fourier domain that is accessible with the chosen configuration and derive the expected resolution of the imager.

In our simulations, we take four resonant illuminations with wavevectors  $\pm \mathbf{k}_{x(y), \text{res}} = \pm n_s k_0 \sin \theta_{\text{res}} \hat{\mathbf{x}}(\hat{\mathbf{y}})$ . We assume that the diffracted field is detected continuously in the  $2\pi$  str solid angle about the

normal to the grating. Using Equations (7) and (8) it is seen that the accessible 2D Fourier domain for the object polarizability is made of eight disks with radius  $n_s k_0$  centered on  $\pm \mathbf{k}_{x(y), \text{res}}$  and  $\pm \mathbf{k}_{x(y), \text{res}} + \mathbf{K}_{-1,0}(\mathbf{K}_{0,-1})$ . Note that, in the absence of the grating, the accessible 2D Fourier domain would be made of four disks with radius  $n_s k_0$  centered on  $\pm \mathbf{k}_{x(y), \text{inc}}$ . The plot of the point spread function of the imager, obtained by Fourier transforming the spectral support, is given in Figure 2. One observes that the resolution is about  $\lambda/10$  in all directions but that the side lobes are particularly important along the diagonals of the grating. In the absence of the grating, i.e. when the objects are deposited on the glass substrate, the resolution is about  $\lambda/5$ .

This simple Fourier analysis holds when the grating field approximations, Equations (2) and (3), hold and when the diffracted field is continuously detected in  $2\pi$  str. In practice, the field is detected along several discrete directions and one cannot totally neglect the higher order terms in the Rayleigh series. Hence, instead of using a direct inverse Fourier procedure, it appears more convenient to use an iterative inversion algorithm based on a conjugate gradient to retrieve the permittivity map of the sample. Moreover, this approach makes it possible to incorporate a priori information on the object and to improve further the resolution of the images.

### 3. Inversion scheme

In this section, we briefly describe the technique that enables us to calculate the scattered far-field for a given

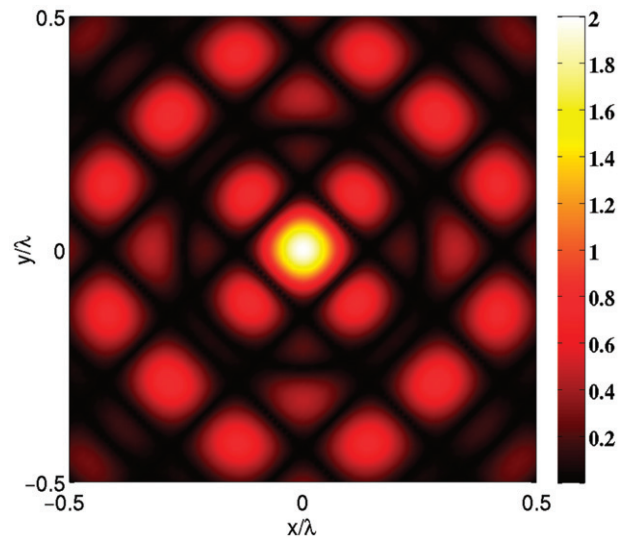


Figure 2. Point spread function versus  $r_{\parallel}/\lambda$ . (The color version of this figure is included in the online version of the journal.)

estimation of the permittivity and the inversion procedure.

### 3.1. Forward scattering problem

Contrary to the first section, the forward scattering problem is addressed rigorously, without assuming Born approximation. In other words, the unperturbed grating field  $\mathbf{E}_{\text{grating}}$  is replaced by the local field  $\mathbf{E}$  that accounts for the presence of the object in Equation (4). The local field is computed through the coupled dipole method (CDM) [22,24]. In this technique, the sample under study is considered a perturbation of the periodically nanostructured substrate. One introduces the field susceptibility tensor  $\mathbf{G}$  such that  $\mathbf{G}(\mathbf{r}, \mathbf{r}')\mathbf{p}$  is the electric field at  $\mathbf{r}$  radiated by a dipole  $\mathbf{p}$  located at  $\mathbf{r}'$  above the grating [24]. Note that

$$\mathbf{G}(\mathbf{r}, \mathbf{r}') = \mathbf{g}(\mathbf{k}, \mathbf{r}') \exp(in_s k_0 r) / r \quad (9)$$

with  $\mathbf{k} = n_s k_0 \hat{\mathbf{r}}$  in far-field (in the substrate). The calculation of  $\mathbf{G}$  can be found in [22,25].

To calculate the local field  $\mathbf{E}$  a volume integral equation restricted to the volume of the scatterer needs to be solved [26]. The scatterer is discretized as a collection of  $K$  dipolar subunits arranged along a cubic array. Each subunit is small enough compared to the spatial variations of the electromagnetic field for the dipole approximation to apply. Then, the electric local field at each subunit position is derived from the self-consistent equation

$$\mathbf{E}(\mathbf{r}_i) = \mathbf{E}_{\text{grating}}(\mathbf{r}_i) + \sum_{k=1, k \neq i}^K \mathbf{G}(\mathbf{r}_i, \mathbf{r}_k) \alpha(\mathbf{r}_k) \mathbf{E}(\mathbf{r}_k), \quad (10)$$

where  $\alpha(\mathbf{r}_k)$  is the polarizability of the subunit located at the position  $\mathbf{r}_k$ ,  $\alpha = d^3 \alpha_d$ .

Once the electric local field is known by solving the linear system represented by Equation (10), the field outside the object can be computed with,

$$\mathbf{E}(\mathbf{r}) = \mathbf{E}_{\text{grating}}(\mathbf{r}) + \sum_{k=1}^K \mathbf{G}(\mathbf{r}, \mathbf{r}_k) \alpha(\mathbf{r}_k) \mathbf{E}(\mathbf{r}_k). \quad (11)$$

In an ODT experiment, the detection is performed in the far-field, which permits us to use the far-field expression of the field susceptibility tensor, Equation (9).

More precisely, the scattered field is measured for  $M$  points of observation and  $L$  different angles of incidence. Then Equation (11) can be rewritten symbolically in the following way:

$$\mathbf{E}_l^d = \mathbf{B} \alpha \mathbf{E}_l, \quad (12)$$

where  $l = 1, \dots, L$ , and  $\mathbf{B}$  is a matrix of size  $(3M \times 3K)$ . The matrix  $\mathbf{B}$  contains the field susceptibility tensors,  $\mathbf{G}(\mathbf{r}_j, \mathbf{r}_k)$ , where  $\mathbf{r}_k$  denotes a point in the discretized object,  $k = 1, \dots, K$ , while  $\mathbf{r}_j$  is an observation point,  $j = 1, \dots, M$ .  $\mathbf{B}$  does not depend on the angle of incidence.  $\alpha \mathbf{E}_l$  is a vector of size  $3K$  which represents, for each angle of incidence, the dipole moment induced at each point of discretization of the object. With this approach, we are able to simulate ‘rigorously’ the field diffracted by any object deposited on the grating in the configuration of the ODT experiment.

### 3.2. Inverse scattering problem

The realm of inverse scattering problems is to determine properties of unknown targets from the knowledge of their responses to known exterior excitation. In electromagnetism, these problems have been extensively studied during the last decades [27–32]. Special sections in the journal *Inverse Problems* devoted to the validation of inversion algorithms against experimental data are reported [33–35] for both two- and three-dimensional cases. Many approaches have been investigated and the most effective ones are iterative techniques. The basic idea underlying these techniques is to start with an initial guess and gradually adjust the parameter of interest, namely the refractive index of the targets, by minimizing a cost functional. This functional describes the discrepancy between measurements (the response to the exterior excitation) and the response, computed via a forward solver, that would be measured if the target under test is the available estimate. In this framework, we have extended these techniques to optical imaging [3,7,9,36,37].

For the optical imaging problem, we consider an unknown target, entirely confined in a bounded box  $\Omega \subset \mathbb{R}^3$  as shown in Figure 1, successively illuminated by  $l = 1, \dots, L$  electromagnetic waves. For each illumination  $l$ , the scattered field  $\Psi_l$  is measured on the surface  $\Gamma$ . The inverse scattering problem consists of finding the complex relative permittivity  $\varepsilon$  distribution in  $\Omega$  such that the corresponding scattering field  $\mathbf{E}_l^d$  matches the measured one. This ill-posed nonlinear problem is solved iteratively. The procedure used in this article has been explained in some references [7,14] but for the convenience of the readers we explain it here briefly. A sequence of polarizabilities  $\{\alpha_n\}$  is constructed according to the following relation

$$\alpha_n = \alpha_{n-1} + a_n d_n, \quad (13)$$

where  $\alpha_n$  and  $\alpha_{n-1}$  denote estimates of the unknown polarizability  $\alpha$  for iteration step  $n$  and  $n - 1$ , respectively.  $d_n$  is an updating direction involving the gradient of the cost functional  $\mathcal{F}(\alpha)$  with respect to  $\alpha$  assuming

that the internal fields  $\mathbf{E}_l$  do not change. The scalar weight  $a_n \in \mathbb{C}$  is determined by minimizing at each iteration step  $n$  the cost functional  $\mathcal{F}_n$  defined as

$$\begin{aligned} \mathcal{F}_n(\alpha_n) &= \frac{\sum_{l=1}^L \|\Psi_l - \bar{\mathbf{B}}\alpha_n \mathbf{E}_{l,n}\|_{\Gamma}^2}{\sum_{l=1}^L \|\Psi_l\|_{\Gamma}^2} \\ &= W_{\Gamma} \sum_{l=1}^L \|\Psi_l - \bar{\mathbf{B}}\alpha_n \mathbf{E}_{l,n}\|_{\Gamma}^2, \end{aligned} \quad (14)$$

with  $\mathbf{E}_{l,n}$  being the local electric field that would be present in  $\Omega$  if the polarizability distribution was  $\alpha_{n-1}$ . The field  $\mathbf{E}_{l,n}$  is obtained by solving the dense linear system described by Equation (10) with the polarizability taken equal to  $\alpha_{n-1}$ . When the objects are much smaller than the wavelength, the renormalized Born approximation [7], i.e.  $\mathbf{E}_{l,n} = \mathbf{E}_{\text{grating}}^l$ , can be successfully used. This assumption greatly diminishes the computational time but it does not account for multiple scattering phenomena. Substituting the expression of the polarizability  $\alpha_n$  derived from Equation (13) in Equation (14) leads to a polynomial expression with respect to the scalar coefficient  $a_n$ . Thus, the minimization of the cost functional  $\mathcal{F}_n$  is reduced to a minimization of a simple cost function  $\mathcal{F}_n(a_n)$ , for which the unique minimum is reached for

$$a_n = \frac{\sum_{l=1}^L \langle \bar{\mathbf{B}}d_n \mathbf{E}_{l,n} | \Psi_l - \bar{\mathbf{B}}\alpha_{n-1} \mathbf{E}_{l,n} \rangle_{\Gamma}}{\sum_{l=1}^L \|\bar{\mathbf{B}}d_n \mathbf{E}_{l,n}\|_{\Gamma}}, \quad (15)$$

where  $\langle \cdot | \cdot \rangle_{\Gamma}$  denotes the inner product in  $L^2$ . As the updating direction  $d_n$ , we take the conjugate gradient direction

$$d_n = g_{n,\alpha} + \gamma_n d_{n-1}, \quad (16)$$

with  $g_{n,\alpha}$  being the gradient of the cost functional  $\mathcal{F}$  with respect to the polarizability assuming that the internal fields  $\mathbf{E}_l$  do not change

$$g_{n,\alpha} = -W_{\Gamma} \sum_{l=1}^L \mathbf{E}_{l,n}^* \cdot \bar{\mathbf{B}}^{\dagger} (\Psi_l - \bar{\mathbf{B}}\alpha_{n-1} \mathbf{E}_l), \quad (17)$$

in which  $\hat{\mathbf{u}}^*$  represents the complex conjugate of  $\hat{\mathbf{u}}$  and  $\bar{\mathbf{B}}^{\dagger}$  denotes the transpose complex conjugate matrix of the matrix  $\bar{\mathbf{B}}$ .

The scalar coefficient  $\gamma_n$  is defined as

$$\gamma_n = \frac{\langle g_{n,\alpha} | g_{n,\alpha} - g_{n-1,\alpha} \rangle_{\Gamma}}{\|g_{n-1,\alpha}\|_{\Gamma}^2}. \quad (18)$$

The initial guess of the iterative algorithm  $\alpha_0$  is estimated with a back-propagation procedure [7].

We now assume that the objects under study have a real relative permittivity that is between 1 and  $\varepsilon_r$ . This a priori information is included in the inversion scheme by retrieving an auxiliary parameter  $\xi$  such that  $\varepsilon = 1 + (\varepsilon_r - 1)e^{-\xi^2}$  instead of retrieving the

polarizability  $\alpha$ . The algorithm is kept as described previously but with a new gradient of  $\mathcal{F}$  with respect to the parameter of interest. This new gradient reads

$$g_{n,\xi} = g_{n,\alpha} \frac{d\alpha}{d\xi}, \quad (19)$$

where  $g_{n,\xi}$  is the gradient of  $\mathcal{F}$  with respect to  $\xi$  and  $g_{n,\alpha}$  is the gradient as given in Equation (17). We use a numerical optimization scheme to zero  $g_{n,\xi}$  and find  $a_n$ .

## 4. Results

In all the numerical experiments, the incident beam is coming from the glass substrate and makes an angle of  $80^\circ$  with respect to the  $z$ -axis to excite, via the  $(-1, 0)$  diffraction order of the grating, the short-range plasmon of the metallic film, see Section 2. We have used eight different illuminations by rotating the incident plane of  $45^\circ$  about the  $z$ -axis. The scattered field is detected in the substrate for 80 angles of observation within a cone of half angle  $70^\circ$ . The synthetic data  $\Psi_l$  are always computed without any approximation with Equations (10) and (11).

All the images are obtained with the nonlinear inversion algorithm that accounts for multiple scattering. Note that the Born approximation fails quickly when high spatial frequency evanescent waves are used to probe the sample [10,14]. To fasten the iterative inversion procedure, the near-field equation, Equation (10) is solved by replacing the grating field susceptibility  $\mathbf{G}$  by a simpler tensor accounting for the multilayer only. On the other hand, the far-field equation Equation (11) is computed with the adequate far-field grating tensor [10]. We have stopped the iteration procedure when the cost function reaches a ‘plateau’. We did not notice any marked change when continuing iterating. The typical number of iterates reported here is 2000, bearing in mind that for simple cases, such as dipoles and when including the a priori information, this number decreases.

### 4.1. Imaging without a priori information

To point out the resolution improvement brought about by the nanostructured substrate, we compare the images of two minute spheres, of relative permittivity 2.25, the centers of which are separated by  $\lambda/10$ . The images are obtained with the same inversion procedure for three different configurations. The spheres are placed in homogeneous space, on a glass substrate and on the grating, see Figures 3(a)–(c), respectively. As expected, one observes that the only spheres placed on the grating can be distinguished. Since the nanostructured substrate is not invariant by translation, it is

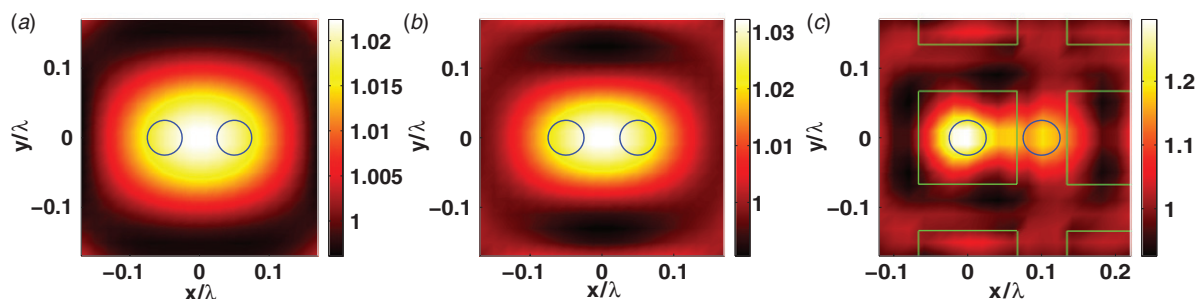


Figure 3. Image of two spheres of radius  $a = \lambda/40$  and interdistance  $\lambda/10$  symbolized by blue circles. Map in the  $(x, y)$  plane at altitude  $z = \lambda/40$  of the real part of the relative permittivity for different configuration. The two spheres are in (a) an homogeneous background, (b) on a glass substrate, (c) on the grating. The grating pads are depicted with green squares. (The color version of this figure is included in the online version of the journal.)

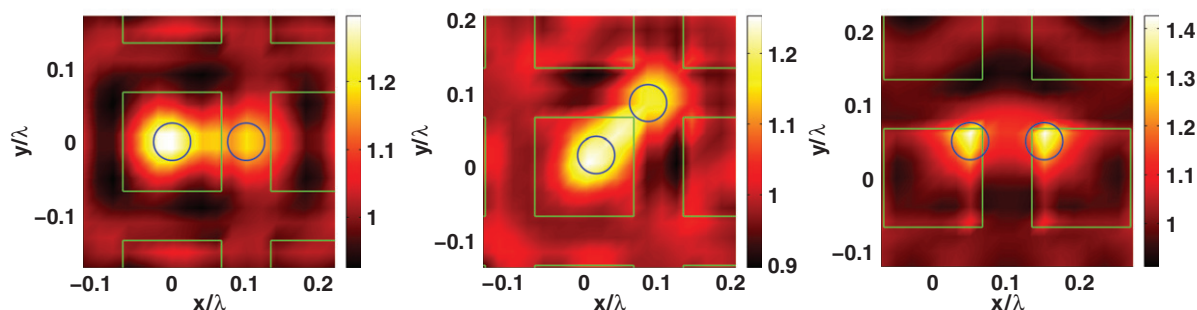


Figure 4. Same as Figure 3, but the two spheres are placed at different positions on the grating. (The color version of this figure is included in the online version of the journal.)

necessary to check that the resolution does not depend too much on the position of the objects on the grating. In Figure 4, we display the images obtained for three different positions of the spheres. Although some differences can be noticed, we are able to distinguish the two spheres in all cases. Note that, as expected from Figure 2, the image is particularly distorted when the spheres are placed along the diagonals of the grating.

We now investigate the ability of the inversion procedure to retrieve more complicated objects. We consider a torus of outer diameter  $\lambda/4.5$ , inner diameter  $\lambda/10$  and height  $\lambda/17$ . The torus is either homogeneous (Figure 5(a), torus of relative permittivity of 2.25) or inhomogeneous (Figure 5(b), torus of relative permittivity of  $\varepsilon = 2.5$  on the left-hand side and of  $\varepsilon = 2 + 0.5i$  on the right-hand side). The torus is placed on the grating in such a way that the resulting geometry does not exhibit any symmetry.

The retrieved map of permittivity of the homogeneous torus is shown in Figure 6. One observes that the resolution decreases as one moves away from the grating so that the inner hole disappears. This was to be expected since the high resolution comes from the  $(-1, 0)$  order of the grating, which is

strongly evanescent. The lack of homogeneity of the torus can be explained by the fact that the near-field calculation in the inverse problem is not performed rigorously. It assumes that the object is deposited on a homogeneous multilayer and thus it does not account for the hot spots that appear at the edges of the grating pads.

Figures 7 and 8 display the real and imaginary parts of the relative permittivity of the inhomogeneous torus. The torus is accurately retrieved and the absorption is clearly localized. Comparing Figure 6 with Figures 7 and 8 shows that the reconstruction is not deteriorated by the presence of inhomogeneous absorption.

#### 4.2. Imaging with a priori information

We now introduce some a priori information in the reconstruction procedure. We assume that the relative permittivity of the objects under study is real and in the range  $[1; 2.25]$ . This knowledge corresponds for example to practical applications in optical imaging of lossless dielectric nanocomponents. Other cases can be considered, with different ranges of permittivity.

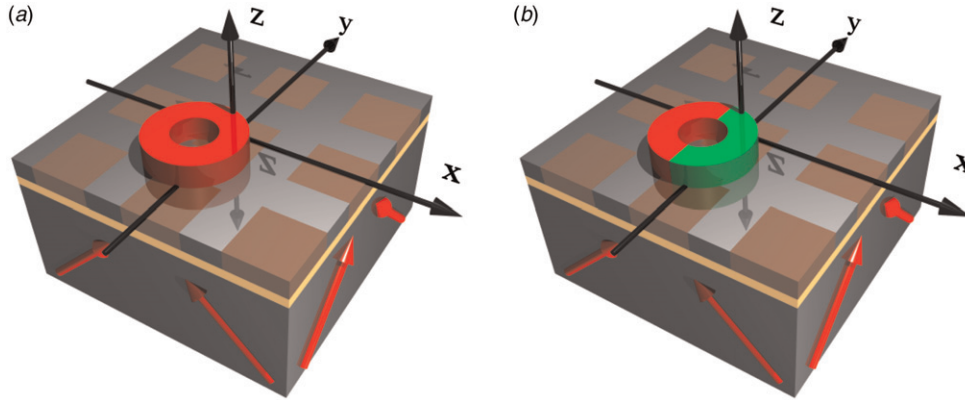


Figure 5. Torus on the nanostructured substrate with outer diameter  $\lambda/4.5$ , inner diameter  $\lambda/10$ , height  $\lambda/17$ . (a) Homogeneous torus of relative permittivity of 2.25. (b) Inhomogeneous torus of relative permittivity  $\epsilon = 2.5$  on the left side and  $\epsilon = 2 + 0.5i$  on the right side.

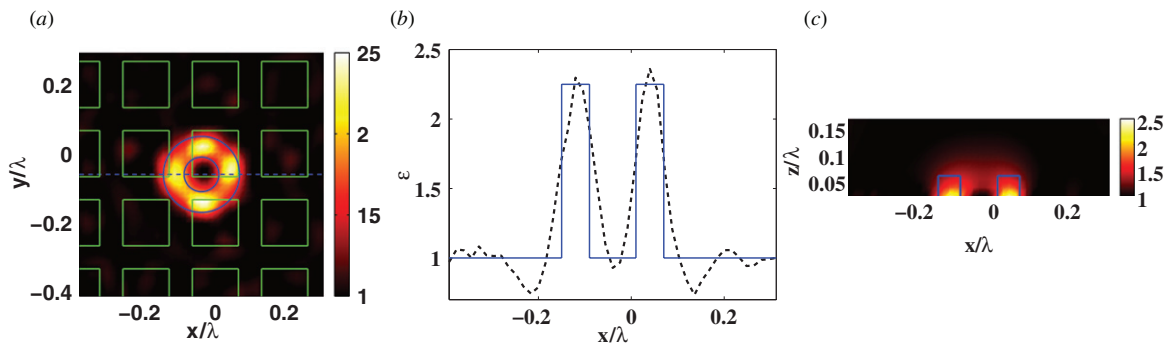


Figure 6. Image of the homogeneous torus. (a) Map of relative permittivity in the  $(x, y)$  plane at  $z = \lambda/125$ . (b) Relative permittivity versus  $x/\lambda$  along the dashed line in (a). (c) Map of relative permittivity in the  $(x, z)$  plane at  $y = 0$ .

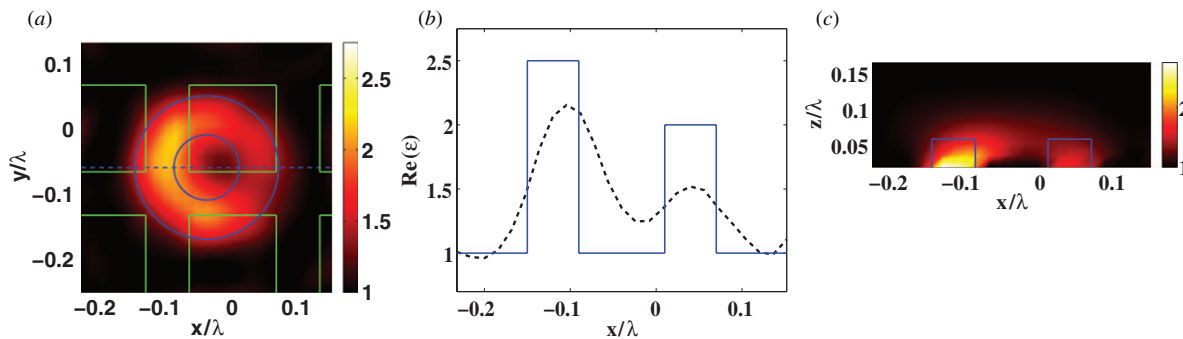


Figure 7. Image of the inhomogeneous torus. (a) Map of the real part relative permittivity in the  $(x, y)$  plane at  $z = \lambda/40$ . (b) Real part relative permittivity versus  $x/\lambda$  along the line plotted in dashed line in (a). (c) Map of the real part of the relative permittivity in the  $(x, z)$  at  $y = 0$ .

The aim of this section is to show that a limitation of the range of permittivity leads, in the inversion procedure, to an improvement of the quality of the reconstructed image. We first consider two minute

spheres of relative permittivity 2.25 with radius  $a = \lambda/40$  separated by a distance of  $\lambda/15$  for three different positions on the grating. The reconstructed map of permittivity displayed in Figure 9 is very accurate

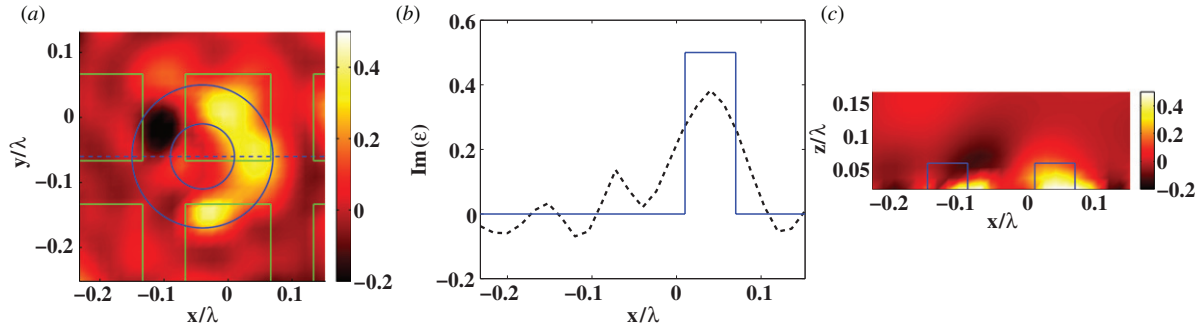


Figure 8. Image of the inhomogeneous torus, same as Figure 7 but for the imaginary part of the relative permittivity. (The color version of this figure is included in the online version of the journal.)

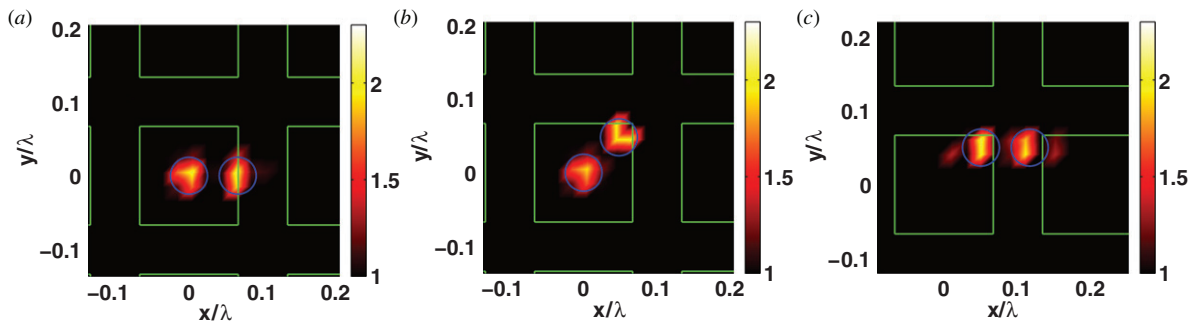


Figure 9. Same as in Figure 4 but the two spheres are separated by a distance of  $\lambda/15$  and use of a priori information. (The color version of this figure is included in the online version of the journal.)

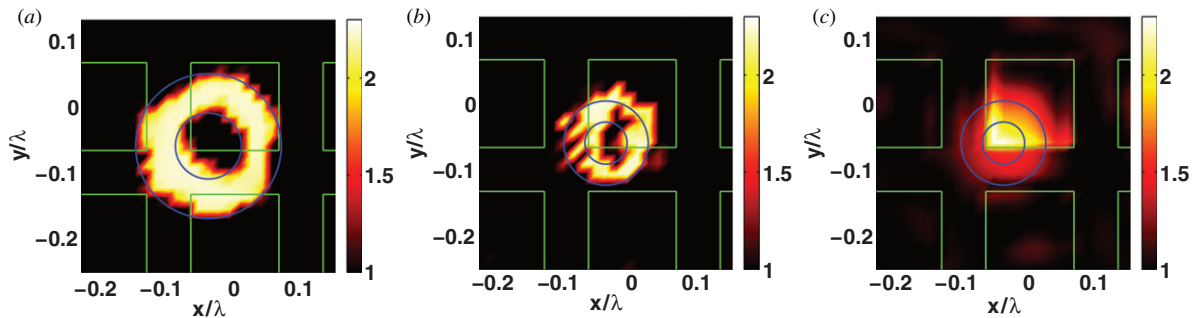


Figure 10. (a) Reconstruction with a priori information for the torus described in Figure 5(a). (b)–(c) Reconstruction with and without a priori information of a torus built with a cylinder of diameter of  $\lambda/8$  and a height of  $\lambda/17$  with a hole inside of  $\lambda/15$  of diameter. (The color version of this figure is included in the online version of the journal.)

whatever the position of the spheres. Note that without the a priori information, the inversion procedure would not be able to distinguish the two spheres. To further point out the improvement brought about by incorporating a priori information in the reconstruction procedure, we display in Figure 10(a) the reconstructed map of permittivity of the homogeneous torus depicted in Figure 5(a). The image of the torus obtained with a priori information is almost perfect. If one decreases the size of the torus down to  $\lambda/7$  for the outer diameter

and  $\lambda/15$  for the inner diameter the reconstructed image with a priori information is still fair (see Figure 10(b)), while that obtained without a priori information does not display the inner hole, see Figure 10(c).

#### 4.3. Robustness with respect to noise

In this section, we analyze the robustness of our inversion scheme when an uncorrelated noise is added

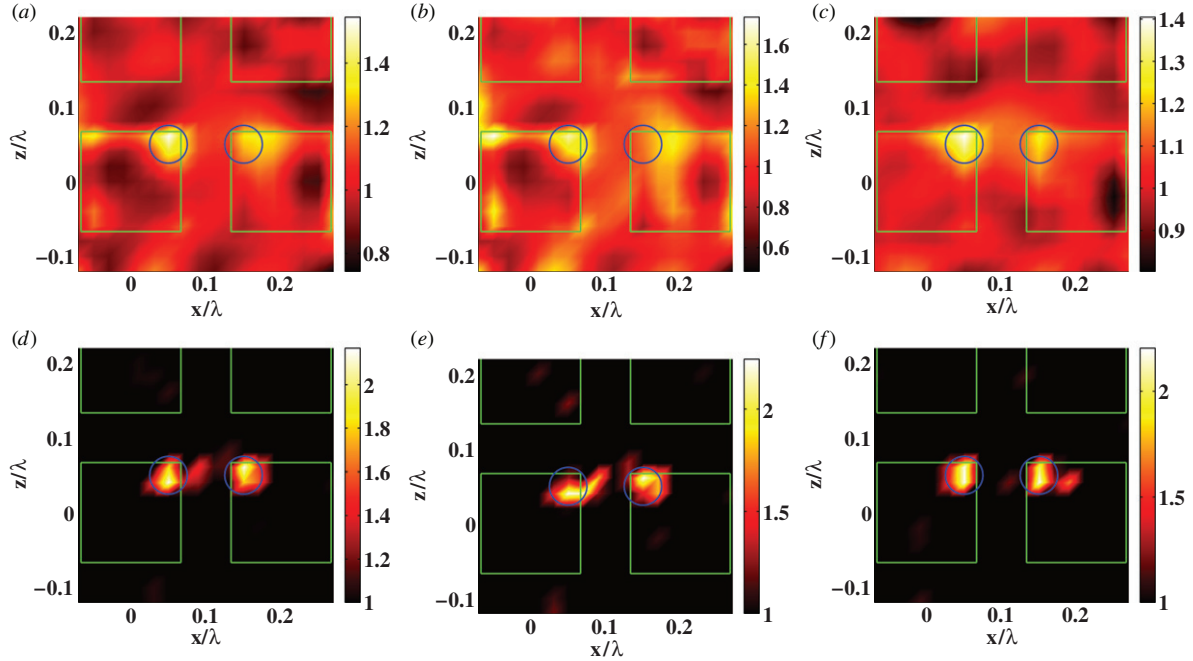


Figure 11. Image of two spheres of radius  $a = \lambda/40$  and interdistance  $\lambda/10$  symbolized by blue circles. Map in the  $(x, y)$  plane at altitude  $z = \lambda/40$  of the real part of the relative permittivity for different noise. With no a priori information: (a) noise A with  $u = 0.05$ ; (b) noise A with  $u = 0.1$ ; (c) noise B with  $u = 0.3$ . With a priori information: (d) noise A with  $u = 0.05$ ; (e) noise A with  $u = 0.1$ ; (f) noise B with  $u = 0.3$ . (The color version of this figure is included in the online version of the journal.)

to the scattered field. We have chosen two kind of noise. The first one (noise A) corrupts each component of the scattered field as,

$$\text{Re}[\tilde{f}_{l,v}(\mathbf{r}_k)] = \text{Re}[f_{l,v}(\mathbf{r}_k)] + uA_r\xi_{l,v} \quad (20)$$

$$\text{Im}[\tilde{f}_{l,v}(\mathbf{r}_k)] = \text{Im}[f_{l,v}(\mathbf{r}_k)] + uA_i\eta_{l,v} \quad (21)$$

where  $v$  stands for the component along the  $x$ ,  $y$ , or  $z$  axes.  $\xi_{l,v}$  and  $\eta_{l,v}$  are random numbers with uniform probability density in  $[-1, 1]$ , and  $u$  is a real number smaller than unity that monitors the level of the noise.  $A_r = \max[\text{Re}(f_{l,v})] - \min[\text{Re}(f_{l,v})]$  and  $A_i = \max[\text{Im}(f_{l,v})] - \min[\text{Im}(f_{l,v})]$ . The second one (noise B) is defined as

$$\text{Re}[\tilde{f}_{l,v}(\mathbf{r}_k)] = \text{Re}[f_{l,v}(\mathbf{r}_k)](1 + u\xi_{l,v}) \quad (22)$$

$$\text{Im}[\tilde{f}_{l,v}(\mathbf{r}_k)] = \text{Im}[f_{l,v}(\mathbf{r}_k)](1 + u\eta_{l,v}). \quad (23)$$

It is obvious from the definition of the two noises that the first one corrupts strongly the weak value of the field.

Figure 11 shows the evolution of the resolution on two dipoles versus different values of  $u$  for the two noises presented in Equations (20) and (22). Notice that for the noise A and value of  $u = 0.1$  (Figure 11(a))

the two dipoles are not retrieved and that the edge of the grating pad appear, while with a priori information (Figure 11(e)) the resolution is achieved. Notice that the images are similar with noise A ( $u = 0.05$ ) and with noise B ( $u = 0.3$ ). This shows that the noise A is more disturbing than the noise B, as mentioned above.

Figure 12 provides the same study but for the homogeneous torus presented in Figure 5(a). One can see that for the larger object, compare with the dipoles, the effect of the noise is stronger. A small value of  $u$  for the noise A does not permit us to retrieve the torus (Figure 12(a)) except when a priori information is used (Figure 12(d)).

For the noise B the torus is only retrieved with  $u = 0.1$  (Figure 12(b)), while with a priori information the torus is perfectly retrieved with  $u = 0.2$ .

## 5. Conclusion

In conclusion, we believe that grating-assisted optical diffraction tomography combined with sophisticated inversion schemes could be a powerful tool for imaging nanometric structures. A simple Fourier analysis shows that a power of resolution about  $\lambda/10$  can be expected with a grating-substrate with period  $\lambda/5$ .

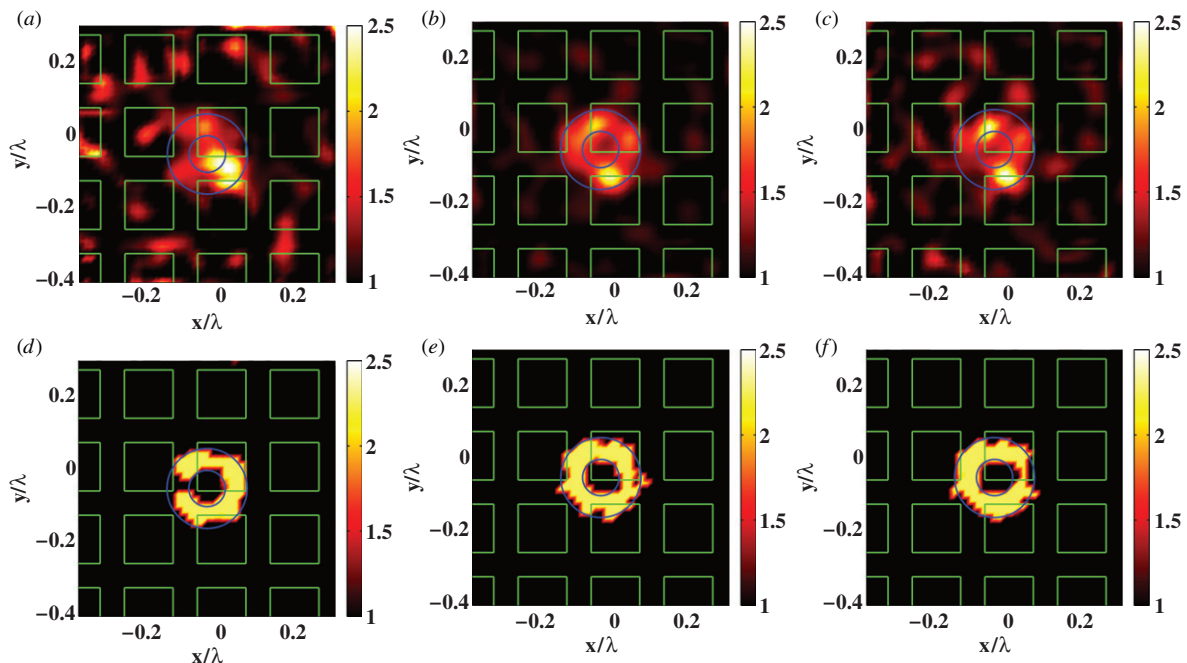


Figure 12. Map of the real part relative permittivity in the  $(x, y)$  plane at  $z = \lambda/40$  for the homogeneous torus presented in Figure 5(a). Without a priori information: (a) noise A with  $u = 0.05$ ; (b) noise B with  $u = 0.1$ ; (c) noise B with  $u = 0.2$ . With a priori information: (d) noise A with  $u = 0.05$ ; (e) noise B with  $u = 0.1$ ; (f) noise B with  $u = 0.2$ . (The color version of this figure is included in the online version of the journal.)

Incorporating a priori information on the range of the relative permittivity of the objects in the reconstruction procedure permits us to ameliorate the resolution up to  $\lambda/15$  and gives a better robustness to the noise.

## References

- [1] Lauer, V. *J. Microsc.* **2002**, *205*, 165–176.
- [2] Debailleul, M.; Simon, B.; Georges, V.; Haeberlé, O.; Lauer, V. *Meas. Sci. Technol.* **2008**, *19*, 074009.
- [3] Chaumet, P.C.; Belkebir, K.; Sentenac, A. *Phys. Rev. B* **2004**, *69*, 245405.
- [4] Haeberlé, O.; Sentenac, A.; Giovannini, H. An Introduction to Diffractive Tomographic Microscopy. In *Modern Research and Educational Topics in Microscopy*; Méndez-Vilas, A., Díaz, J., Eds.; Formatex: Badajoz, Spain, 2007; pp 956–967.
- [5] Streibl, N. *J. Opt. Soc. Am. A* **1985**, *2*, 121–127.
- [6] Carney, P.S.; Schotland, J.C. *J. Opt. Soc. Am. A* **2003**, *20*, 542–547.
- [7] Belkebir, K.; Chaumet, P.C.; Sentenac, A. *J. Opt. Soc. Am. A* **2005**, *22*, 1889–1897.
- [8] Ippolito, S.B.; Goldberg, B.B.; Ünlü, M.S. *Appl. Phys. Lett.* **2001**, *78*, 4071–4073.
- [9] Sentenac, A.; Chaumet, P.C.; Belkebir, K. *Phys. Rev. Lett.* **2006**, *97*, 243901–4.
- [10] Chaumet, P.C.; Belkebir, K.; Sentenac, A. *Phys. Rev. A* **2007**, *76*, 013814–7.
- [11] Alexandrov, S.A.; Hillman, T.R.; Gutzler, T.; Sampson, D.D. *Phys. Rev. Lett.* **2006**, *97*.
- [12] Debailleul, M.; Georges, V.; Simon, B.; Morin, R.; Haeberlé, O. *Opt. Lett.* **2009**, *34*, 79–81.
- [13] Choi, W.; Fang-Yen, C.; Badizadegan, K.; Oh, S.; Lue, N.; Dasari, R.R.; Feld, M.S. *Nat. Methods* **2007**, *4*, 717–719.
- [14] Chaumet, P.C.; Belkebir, K.; Sentenac, A. *Opt. Lett.* **2004**, *29*, 2740–2742.
- [15] Maire, G.; Drsek, F.; Girard, J.; Giovannini, H.; Talneau, A.; Konan, D.; Belkebir, K.; Chaumet, P.C.; Sentenac, A. *Phys. Rev. Lett.* **2009**, *102*, 213905.
- [16] Belkebir, K.; Chaumet, P.C.; Sentenac, A. *J. Opt. Soc. Am. A* **2006**, *23*, 586–595.
- [17] Simonetti, F. *Phys. Rev. E* **2006**, *73*, 036619.
- [18] Sentenac, A.; Guérin, C.A.; Chaumet, P.C.; Drsek, F.; Giovannini, H.; Bertaux, N.; Holschneider, M. *Opt. Express* **2007**, *15*, 1340–1347.
- [19] Chaumet, P.C.; Belkebir, K.; Sentenac, A. *J. Appl. Phys.* **2009**, *109*, 034901.
- [20] Li, L. *J. Opt. Soc. Am. A* **1997**, *14*, 2758–2767.
- [21] Greffet, J.J.; Carminati, R. *Prog. Surf. Sci.* **1997**, *56*, 133–237.
- [22] Chaumet, P.C.; Sentenac, A. *Phys. Rev. B* **2005**, *72*, 205437–8.

- [23] Fehrembach, A.L.; Enoch, S.; Sentenac, A. *Appl. Phys. Lett.* **2001**, *79*, 4280–4282.
- [24] Chaumet, P.C.; Rahmani, A.; Bryant, G.W. *Phys. Rev. B* **2003**, *67*, 165404.
- [25] Chaumet, P.C.; Rahmani, A. *J. Quant. Spectrosc. Ra.* **2009**, *110*, 22–29.
- [26] Kahnert, F.M. *J. Quant. Spectrosc. Ra.* **2003**, *79–80*, 775–824.
- [27] Belkebir, K.; Kleinman, R.E.; Pichot, C. *IEEE T. Microw. Theory* **1997**, *45*, 469–476.
- [28] Chew, W.C.; Wang, Y.M. *IEEE T. Med. Imaging* **1990**, *9*, 218–225.
- [29] Joachimowicz, N.; Pichot, C.; Hugonin, J.P. *IEEE T. Antenn. Propag.* **1991**, *39*, 1742–1753.
- [30] Roger, A. *IEEE T. Antenn. Propag.* **1981**, *29*, 232–238.
- [31] van den Berg, P.M.; van Broekhoven, A.L.; Abubakar, A. *Inverse Probl.* **1999**, *15*, 1325–1344.
- [32] Souriau, L.; Duchêne, B.; Lesselier, D.; Kleinman, R.E. *Inverse Probl.* **1996**, *12*, 463–481.
- [33] Belkebir, K.; Saillard, M. *Inverse Probl.* **2001**, *17*, 1565–1571.
- [34] Belkebir, K.; Saillard, M. *Inverse Probl.* **2005**, *21*, S1–S3.
- [35] Litman, A.; Crocco, L. *Inverse Probl.* **2009**, *25*, 020201.
- [36] Chaumet, P.C.; Belkebir, K. *Inverse Probl.* **2009**, *25*, 024003.
- [37] Belkebir, K.; Sentenac, A. *J. Opt. Soc. Am. A* **2003**, *20*, 1223–1229.